Hot chemistry and physics in the planet-forming zones of disks

Bast, J.E.

Citation

Bast, J. E. (2013, January 10). *Hot chemistry and physics in the planet-forming zones of disks*. Retrieved from https://hdl.handle.net/1887/20396

Author: Bast, Jeanette Elisabeth
Title: Hot chemistry and physics in the planet-forming zones of disks
Issue Date: 2013-01-10

V

Exploring organic chemistry in planet-forming zones[1]

Context. Over the last few years, the chemistry of molecules other than CO in the planet-forming zones of disks is starting to be explored with Spitzer and high-resolution ground-based data. However, these studies have focused only on a few simple molecules.
Aim. The aim of this study is to put observational constraints on the presence of more complex organic and sulfur-bearing molecules predicted to be abundant in chemical models of disks.
Methods. High S/N Spitzer spectra at 10–30 μm of the near edge-on disks IRS 46 and GV Tau are used to search for mid-infrared absorption bands of various molecules. These disks are good laboratories because absorption studies do not suffer from low line/continuum ratios that plague emission data. Simple LTE slab models are used to infer column densities and excitation temperatures for detected lines and upper limits for non-detections.
Results. Mid-infrared bands of HCN, C_2H_2 and CO_2 are clearly detected toward both sources. As found previously for IRS 46 by Lahuis et al. (2006), the HCN and C_2H_2 absorption arises in warm gas with excitation temperatures of 400–700 K, whereas the CO_2 absorption originates in cooler gas of ~250 K. Absolute column densities and their ratios are comparable for the two sources. No other absorption features are detected at the 3σ level. Column density limits of the majority of molecules predicted to be abundant in the inner disk — C_2H_4, C_2H_6, C_6H_6, C_3H_4, C_4H_2, CH_3, HNC, HC_3N, CH_3CN, NH_3 and SO_2—are determined. Simulations are also performed for future higher spectral resolution instruments such as on

---

[1] Based on: J.E. Bast, F. Lahuis, E.F Dishoeck and A.G.G.M. Tielens, 2012, submitted to A&A.

JWST, SOFIA, SPICA or ELTs.
Conclusions. The inferred abundance ratios and limits with respect to C_2H_2 and HCN are roughly consistent with models of the chemistry in high temperature gas. Models of UV irradiated disk surfaces generally agree better with the data than pure X-ray models. The limit on NH_3/HCN implies that evaporation of NH_3-containing ices is only a minor contributor. The inferred abundances and their limits also compare well with those found in comets, suggesting that part of the cometary material derives from warm inner disk gas. Future higher resolution data will provide up to an order of magnitude deeper tests of the models.

5.1 Introduction

The chemical composition of the gas in the inner regions of circumstellar disks plays an important role in determining the eventual composition of the comets and atmospheres of any planets that may form from that gas (see reviews by Prinn 1993, Ehrenfreund & Charnley 2000, Markwick & Charnley 2004, Bergin 2009). In the last few years, observations with the *Spitzer Space Telescope* have revealed a rich chemistry in the inner few AU of disks around low-mass stars, containing high abundances of HCN, C_2H_2, CO_2, H_2O and OH (Lahuis et al. 2006, Carr & Najita 2008, Salyk et al. 2008, Pascucci et al. 2009, Carr & Najita 2011, Kruger et al. 2011, Najita et al. 2010, Pontoppidan et al. 2010, Salyk et al. 2011). Spectrally and spatially resolved data of CO using ground-based infrared telescopes at 4.7 μm show that the warm molecular gas is indeed associated with the disk (e.g., Najita et al. 2003, Brittain et al. 2003, 2007, 2009, Blake & Boogert 2004, Pontoppidan et al. 2008, Salyk et al. 2011b, Brown et al. subm.), with in some cases an additional contribution from a disk wind (Bast et al. 2011, Pontoppidan et al. 2011). Spectrally resolved ground-based observations have also been obtained of OH and H_2O at 3 μm (Carr et al. 2004, Mandell et al. 2008, Salyk et al. 2008, Fedele et al. 2011), and most recently of HCN and C_2H_2 (Gibb et al. 2007, Doppmann et al. 2008, Mandell et al. 2012). All of these data testify to the presence of an active high-temperature chemistry in the upper layers of disks that drives the formation of OH, H_2O and small organic molecules. However, it is currently not known whether this gas contains more complex organic molecules which may eventually become part of exoplanetary atmospheres.

Observations of large interstellar molecules are usually carried out using (sub-)millimeter telescopes. A wide variety of complex organic species have been found in low- and high-mass protostars at the stage when the source is still embedded in a dense envelope (see Herbst & van Dishoeck 2009,for review). For disks, the pure rotational lines of CO, H_2O, HCO^+, H_2CO, HCN, N_2H^+, CN, C_2H, SO, DCO^+ and DCN have been reported but more complex molecules have not yet been detected (e.g., Dutrey et al. 1997, Kastner et al. 1997, Thi et al. 2004, Fuente et al. 2010, Henning et al. 2010, Öberg et al. 2011, Hogerheijde et al. 2011). Although these millimeter data have the advantage that they do not suffer from dust extinction and can thus probe down to the midplane, current facilities are only sensitive to the cooler gas in the outer disk (> 50AU). Even the Atacama Large Millimeter/submillimeter Array (ALMA) with its much improved spatial resolution and sensitivity can only readily image molecules at ~5 AU or larger in the nearest disks. Moreover, ALMA cannot detect molecules without a permanent dipole moment such as C_2H_2 and CH_4, which are among the most abundant species in the inner disk. Results so far show that there is no clear correlation between the chemistry in the inner and outer parts of the disk (Öberg et al. 2011). The chemistry in the inner regions seems to be sensitive to different shapes of radiation fields and the accretion luminosities (Pascucci et al. 2009, Pontoppidan et al. 2010), but these quantities do not seem to have an impact on the chemical composition of the colder gas further out in the disk.

Searches for more complex molecules in the inner few AU must therefore rely on infrared techniques. However, the strong mid-infrared continuum implies very low line/continuum ratios for emission lines, even at high spectral resolution. Indeed, the recent VLT-CRIRES ($R = \lambda/\Delta\lambda = 10^5$) searches in the 3 μm atmospheric window show that lines of molecules other than CO have line/continuum ratios of typically only a few %, and that even relatively simple species like CH_4 are not detected at the ~1% level (Mandell et al. 2012). On the other hand, absorption lines offer a much better chance of detecting minor species for a variety of reasons. First, absorption occurs from the ground vibrational level where the bulk of the population resides, so that the signal is much less sensitive to temperature. Another advantage is that absorption lines are relative in strength to the continuum whereas emission lines are absolute. So the strength of the absorption lines relative to the continuum will stay the same in sources which have a stronger continuum whereas the emission lines will be dominated by the continuum. Both these advantages imply that absorption lines are easier to detect for less abundant molecular species than emission lines.

Detection of absorption lines requires, however, a special orientation of the disk close to edge-on, so that the line of sight to the continuum passes through the inner disk. Only a few disks have so far been found with such a favorable geometry: that around Oph-IRS46 (Lahuis et al. 2006), GV Tau N (Gibb et al. 2007, Doppmann et al. 2008) and DG Tau B (Kruger et al. 2011). In all cases, the mid-infrared absorption bands of HCN, C_2H_2 and CO_2 have depths of 5–15%, even at the low spectral resolution $R \approx 600$ of *Spitzer*. For high $S/N > 100$ spectra, detection of absorption features of order 1% should be feasible, providing a dynamic range of up to an order of magnitude in abundances to search for other molecules. With increased spectral resolution and sensitivity offered by future mid-infrared instruments such JWST-MIRI ($R \approx 3000$), and SOFIA, SPICA and ELTs ($R \geq 50000$), another order of dynamic range will be opened up.

A large variety of increasingly sophisticated physico-chemical models of the inner regions of disks exist (e.g., Willacy et al. 1998, Aikawa et al. 1999, Markwick et al. 2002, Nomura et al. 2007, Agúndez et al. 2008, Gorti & Hollenbach 2008, Glassgold et al. 2009, Nomura et al. 2009, Willacy & Woods 2009, Woitke et al. 2009, Kamp et al. 2010, Walsh et al. 2010, Aresu et al. 2011, Gorti et al. 2011, Heinzeller et al. 2011, Najita et al. 2011, Vasyunin et al. 2011, Walsh et al. 2012). The models differ in their treatments of radiation fields (UV and/or X-rays), the gas heating and resulting disk structure, dynamical processes such as accretion flows and disk winds, grain properties and chemical networks (e.g., grain opacities, treatment of gas-grain chemistry including H_2 formation at high temperature). Some models consider only the simplest molecules in the chemistry, others have a large chemical network but publish primarily results for species that can be observed at millimeter wavelengths. Only Markwick et al. (2002) list the most abundant species, including complex molecules that do not have a dipole moment, at 1, 5 and 10 AU as obtained from vertically integrated column densities. Since infrared observations probe only part of the disk down to where the continuum becomes optically thick, these models may not be representative of the surface layers. Column densities appropriate for comparison with infrared data have been presented by Agúndez et al. (2008), Najita et al. (2011) but do not provide data for more complex molecules. Woods & Willacy (2007) and Kress et al. (2010) consider PAH processing in the inner disk and study its impact on the abundances of related species like benzene and C_2H_2. Note that PAHs are generally not detected in disks around T Tauri stars, including the two disks studied here, at levels a factor of 10–100 lower than found in the interstellar medium (Geers et al. 2006, Oliveira et al. 2010).

Observations of molecules in comets provide another interesting data set for comparison with protoplanetary disks. Solar system comets were likely formed at distances of about 5–30 AU in the protosolar nebula. Many volatile molecules are now routinely observed in cometary atmospheres at infrared and millimeter wavelengths, including species as complex as C_2H_6, CH_3OH, and even $(CH_2OH)_2$ (see Mumma & Charnley 2011, Bockelée-Morvan 2011,for reviews). It is still debated whether the abundances measured in comets directly reflect those found in the dense envelopes around protostars or whether they result from processing and mixing material from the inner and outer disk into the comet-forming zone. Putting constraints on the inner disks abundances of these molecules will be important to probe the evolution of material from the natal protosolar nebula to the formation of icy bodies.

In this study we use the existing high *S/N Spitzer* spectra of IRS 46 and GV Tau to, for the first time, put upper limits on various molecules in the inner disk: HNC, CH_3, C_2H_4, C_2H_6, C_3H_4, HC_3N, C_6H_6, NH_3, C_4H_2, CH_3CN, H_2S and SO_2. These molecules were selected to include most of the top 15 highest vertical column density molecules at 1 and 5 AU by Markwick et al. (2002). The selected species can in principle directly test the predictions of models of inner disk chemistry. The list also contains several molecules observed in cometary atmospheres and two more molecules with a permanent dipole moment, HNC and HC_3N, which together with HCN can be observed at both infrared and millimeter wavelengths and can thus be used to connect the inner and outer disk chemistries through ALMA imaging.

The mid-infrared spectra of IRS 46 and GV Tau contain detections of C_2H_2, CO_2 and HCN which are analyzed here in terms of column densities and abundances, following the same strategy as for IRS 46 in Lahuis et al. (2007). The earlier detections of HCN and C_2H_2 toward GV Tau were performed in the 3 μm window with higher spectral resolution (Gibb et al. 2007).

A description of the observations and the reduction of the data for IRS 46 and GV Tau is presented in Section 5.2 together with some information about these two protoplanetary disks. Section 5.3.1 presents an overview of the observed and modeled spectra, whereas 5.3.2 uses a synthetic local thermodynamic equilibrium (LTE) model to estimate column densities and excitation temperatures for HCN, C_2H_2 and CO_2 toward GV Tau and compares the results with those for IRS 46.

Section 5.3.3 presents the upper limits for the various molecules toward the two sources and Section 5.3.4 shows how future instruments can provide more stringent limits. Discussion and comparison to chemical models is performed in Section 5.4. A summary of the main conclusions is found in Section 5.5.

5.2 Observations

5.2.1 IRS 46 and GV Tau

The observations of IRS 46 and GV Tau were made using *Spitzer*-IRS in both the Short-High (SH; $9.9 - 19.6\,\mu$m) and Long-High (LH; $18.7 - 37.2\,\mu$m) modes with a spectral resolving power of $R = \lambda/\delta\lambda = 600$.

Oph-IRS 46 was observed at $\alpha = 16^h27^m29^s.4$ and $\delta = -24^o39'16''.3$ (J2000), located in the Ophiuchus molecular cloud at a distance of around 120 pc (Loinard et al. 2008). IRS 46 was initially observed in 2004 as part of the Cores to Disks *Spitzer* legacy program (Evans et al. 2003) and in 2008 and 2009 at multiple epochs to search for variability. Its mid-infrared spectral energy distribution rises strongly with wavelength, as expected for a near edge-on disk (Crapsi et al. 2008). Strong HCN, C_2H_2 and CO_2 absorption has been detected with *Spitzer* and attributed to arise from warm gas in the surface layers of the inner few AU of the disk, seen in absorption against the continuum produced by the hot inner rim on the near and far side of the star (Lahuis et al. 2006). Lahuis et al. (2011,and in prep.) show that hot water emission lines are also detected. More interestingly, strong variation in the depth of the molecular absorption bands as well as in the strength of the water emission lines and the mid-IR contiuum is observed on timescales of a few years. The data used here are the original observations obtained on August 29, 2004 as part of AOR# 0009829888 and published by Lahuis et al. (2006). These show the deepest molecular absorptions, thus providing the best upper limits of column densities of other species relative to the observed C_2H_2, HCN and CO_2 column densities.

GV Tau is a T Tauri star that is partly embedded in the L1524 molecular cloud. Its observations were positioned at $\alpha = 4^h29^m25^s.8$ and $\delta = +24^o33'00''5$ (J2000). It has an infrared companion about 1.2″ to the north. The companion is named GV Tau N and the primary optical source is called GV Tau S. Gibb et al. (2007) detected HCN and C_2H_2 toward GV Tau N using Keck-NIRSPEC at L-band, however, no such detections were made toward GV Tau S. GV Tau has subsequently been observed using the IRS SH mode at multiple epochs with *Spitzer* in a GO4 program (PI, F.Lahuis; program ID 50532). For the SH part of the spectrum the GO4 data (AOR # 0022351616, 0028247808, 0028247552 and 0031618304) were used. For the LH part, data from the *Spitzer* GTO program observed on 02 March 2004 as part of AOR # 0003531008 were adopted. Note that the *Spitzer*-IRS aperture does not resolve the GV Tau binary, in contrast to NIRSPEC. The *Spitzer* spectra therefore combine emission and absorption of GV Tau N and GV Tau S.

Both GV Tau N and GV Tau S are variable at 2 μm (Leinert et al. 2001, Koresko et al. 1999) and at 8 – 13 μm (Przygodda 2004, Roccatagliata et al. 2011). This variability has been attributed to variable accretion mechanisms for GV Tau N and variation in the extinction due to inhomogeneities in the circumstellar material for GV Tau S (Leinert et al. 2001). However, the multi-epoch *Spitzer* data do not show significant mid-infrared variation on timescales of a few months up to a few years, in contrast with IRS 46. The continuum of GV Tau N is about an order of magnitude brighter than the continuum of GV Tau S between 8 – 13 μm (Przygodda 2004, Roccatagliata et al. 2011). The factor changes between 5 – 10 due to variations in the continuum emission from both the northern and southern source. Since no absorption was seen in GV Tau S in Gibb et al. (2007), Doppmann et al. (2008) it is assumed that the majority of the absorption arises toward GV Tau N. However, the continuum emission from the southern source captured in the *Spitzer*-IRS aperture slightly reduces the total optical depth of the absorption lines in the spectrum. To put an upper limit on the added uncertainty caused by the additional continuum emission from GV Tau S, it is assumed that the mid-IR continuum of GV Tau N is at least 5 times stronger than that of GV Tau S, resulting in an additional uncertainty of $\sim 1 - 4\,\%$ for features that are $\sim 5 - 20\,\%$ deep. Since the effect is minor, no correction is made for the column densities derived here.

5.2.2 Data reduction

The data reduction started with the BCD (Basic Calibrated Data) images from the *Spitzer* archive processed through S18 pipeline. The BCD images were then processed using the Cores to Disks (c2d) analysis pipeline (Lahuis et al. 2006b, Kessler-Silacci et al. 2006). The main processing steps are background correction, bad-pixel removal, spectral extraction, defringing, order matching and spectral averaging. Two extraction methods were used; 1) a full aperture extraction from the BCD images and 2) an optimal extraction using an analytical psf (Lahuis et al. 2007) defined using a set of high S/N calibration stars. For both extractions a relative spectral response function (RSRF) calibration is applied with ξ Dra as the main reference star using MARCS models taken from the *Spitzer* science center (Decin et al. 2004).

For all observations the extraction method giving the best S/N was used to produce the final spectra. The two (partly) independent extraction methods further allow to better discriminate between artifacts and true science features.

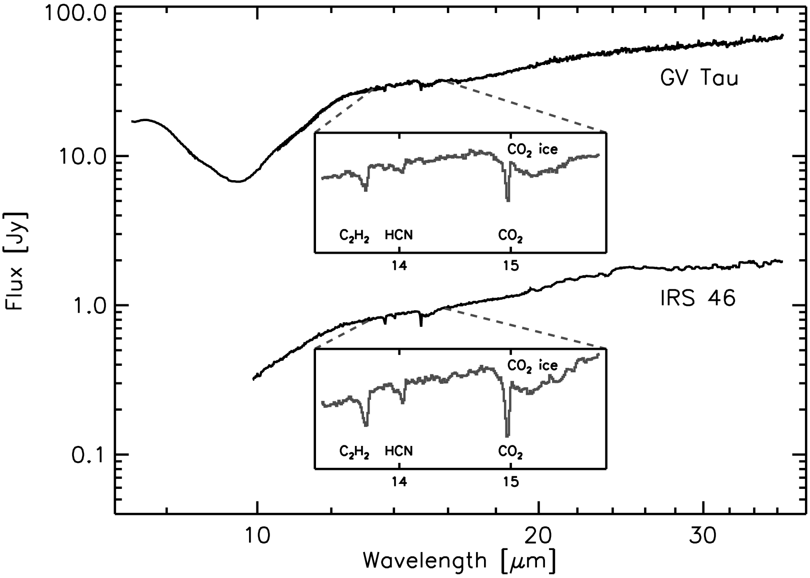

Figure 5.1 Spectra of the protoplanetary disks around IRS 46 and GV Tau taken with the *Spitzer*-IRS.

5.3 Results

5.3.1 Spectra

Figure 5.1 shows the spectra of IRS 46 and GV Tau over the 10 – 37 μm region. The absorption bands of gaseous C_2H_2 ν_5, HCN ν_2 and CO_2 ν_2 can be clearly seen at 13.7, 14.0 and 15.0 μm, together with the solid CO_2 feature at 15 – 16 μm. To search for other molecules, a local continuum has been fitted to the broad spectral features and divided out. The S/N on the continuum is typically 100 or better. No other obvious absorption features are detected at the few % absorption level. The model spectra with derived column densities and upper limits are described below.

5.3.2 C_2H_2, HCN and CO_2

To extract quantitative information from the spectra, a simple local thermodynamical equilibrium (LTE) absorption slab model has been used to fit the data. The free parameters in the model are the excitation temperature, the integrated column density along the line of sight and the intrinsic line width, characterized by the Doppler *b*-value. The excitation temperature sets the level populations of the molecule using the Boltzmann distribution. The lack of collisional rate coefficients for many of the species considered here prevents non-LTE analyses. The model spectrum is convolved with the spectral resolution of the instrument and resampled to the observed spectra. More details about the model and the molecular parameters and data that are used for the three detected molecules can be found in Lahuis & van Dishoeck (2000), Lahuis et al. (2007), Boonman et al. (2003) and in Table 1.

Table 5.1 Basic molecular data

Molecule	Formula	Band	$\tilde{\nu}$[a] [cm^{-1}]	S_{lit}[a] [atm^{-1} cm^{-2}]	S_{int}[b] [atm^{-1} cm^{-2}]	Source[c]
Acetylene	C_2H_2	ν_5 CH bending	729.1	630	816	H08
Carbon Dioxide	CO_2	ν_2 bending	667.4	200	249	H08
Hydrogen Cyanide	HCN	ν_2 bending	713.5	257	286	H08
Hydrogen Isocyanide	HNC	ν_2 bending	464.2	1570	798	G09
Methyl Radical	CH_3	ν_2 out-of-plane bending	606.5	611	616	FPH
Ethylene	C_2H_4	ν_7 CH2 waggling	949.2	324	320	G09
Ammonia	NH_3	ν_2 symmetric bendng	950.0	568	614	H08
Sulphur Dioxide	SO_2	ν_2 bending	517.6	113	97	G09
Ethane	C_2H_6	ν_9 CH3 rocking	822.0	36	29	H08
Diacetylene / Butadiyne	C_4H_2	ν_8 CH bending	627.9	437	229	G09
Benzene	C_6H_6	ν_4 CH bending	673.5	250	212	G09
Propyne / Methyl Acetylene	C_3H_4	ν_9 CH bending	638.6	360	201	G09
Cyanoacetylene / Propynenitrile	HC_3N	ν_5	663.4	278	94	G09
Methyl Cyanide / Acetonitrile	CH_3CN	ν_4 CC stretch	920.3	6	3	G09

[a] Central wavenumber of band and band strengths from *Constants for molecules of astropysical interest in the gas phase* by J. Crovisier
http://wwwusr.obspm.fr/~crovisie/basemole/

[b] Band strength of the simulated spectra. $S = N_L \times \int \tau(\nu)\delta\nu \,/\, n$, (see App. A.1 Helmich 1996). Calculations were performed for $T = 298\,\mathrm{K}$, $b = 20\,\mathrm{km\,s^{-1}}$ and $n = 1 \cdot 10^{15}\,\mathrm{cm^{-2}}$ at a resolution of 3000 to keep all bands far from saturation

[c] H08: HITRAN 2008 (Rothman et al. 2009), G09: GEISA 2009 (Jacquinet-Husson et al. 2011) and FPH: Helmich (1996)

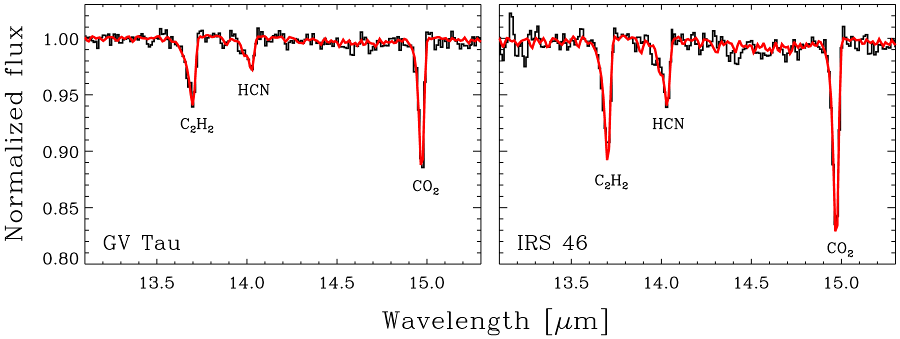

Figure 5.2 Continuum normalized spectra of GV Tau and IRS 46. Plotted in black are the observed spectra and overplotted in red the best-fit synthetic spectra to the absorption bands of C_2H_2 ν_5=1–0, HCN ν_2=1–0 and CO_2 ν_2=1–0. See Table 5.2 for best fit model parameters.

Figure 5.2 presents a blow-up of the $13 - 15\,\mu$m range of the GV Tau and IRS 46 spectra with the continuum divided out. Included are the best-fitting model spectra. The figure clearly shows that the *P*- and *R*-branch lines are difficult to detect at the *Spitzer*-IRS spectral resolution of $R = 600$, however the *Q*-branches of C_2H_2, HCN and CO_2 are easily seen. In addition the *Q*-branch changes its form and depth with excitation temperature and column density. In particular, the depth of the *Q*-branch decreases with increased excitation temperature for the same total column density and broadens to the blue side due to an increase in the population of the higher rotational levels. A higher column density on the other hand increases the central depth of the *Q*-branch since more molecules absorb photons. As can be seen in Lahuis & van Dishoeck (2000) the *Q*-branch is sensitive to the adopted Doppler *b*-value with the magnitude of the effect depending on the temperature and column density. The C_2H_2 lines become more easily optically thick than those of the other molecules at lower temperatures so care should be taken. Spectrally resolved data obtained with Keck-NIRSPEC (Salyk et al. 2011b, Lahuis et al. 2006) and within our VLT-CRIRES survey (Pontoppidan et al. 2011b, Brown et al. subm.) show that the HCN and CO lines have $b \approx 12$ km s^{-1}. In our analysis we therefore adopt a Doppler *b*-value of 10 km s^{-1}. This means that at typical temperatures of ~400 K saturation plays a role for column densities above 4 and 15 $\times 10^{16}$ cm^{-2} for C_2H_2 and HCN, respectively. For CO_2 the saturation limit is significantly higher.

A grid of synthetic spectra of C_2H_2, HCN and CO_2 was made for a range of column densities and temperatures and fitted to the data obtained for GV Tau. The best fit as presented in Fig. 5.2 was determined by finding the minimum difference between data and model as measured by the χ^2 values. The derived column

Table 5.2 Results from molecular fits to GV Tau and IRS 46 absorption features

	Temperature [K]		Column density [10^{16} cm^{-2}]	
Source	IRS 46	GV Tau	IRS 46	GV Tau
C_2H_2	$490 \pm^{50}_{30}$	$720 \pm^{60}_{40}$	2.1 ± 0.4	1.4 ± 0.3
HCN	$420 \pm^{40}_{25}$	$440 \pm^{40}_{30}$	3.7 ± 0.8	1.8 ± 0.4
CO_2	$250 \pm^{25}_{15}$	$250 \pm^{25}_{15}$	8.4 ± 1.1	5.1 ± 0.7

densities and excitation temperatures for the different molecules are summarized in Table 5.2. For IRS 46, the values are consistent with those of Lahuis et al. (2006) within the error bars. It is seen that the temperatures of the different molecules and their column density ratios are comparable between GV Tau and IRS 46. This supports the hypotheses that both sources are inclined disks with similar characteristics. In both sources CO_2 has the highest column density but the lowest temperature, whereas the HCN/C_2H_2 ratio is slightly above unity. In their 2 – 5 μm study, Gibb et al. (2007) however find significantly lower temperatures for C_2H_2 (170 ± 20 K) and HCN (115 ± 20 K) compared to our estimated temperatures of about 400 to 700 K. However in later Keck-NIRSPEC L-band observations, Doppmann et al. (2008), Gibb & Troutman (2011) detect lines out to much higher J values, indicating warmer gas around 500 K. Our mid-infrared results are therefore not inconsistent with the near-IR data.

The high resolution near-IR data for IRS 46 and GV Tau N show that the spectral lines are shifted in velocity. For IRS46, CO and HCN are blueshifted by about 24 km s^{-1} with respect to the cloud (Lahuis et al. 2006) whereas for GV Tau the HCN lines are redshifted by about 13 km s^{-1} compared with the star (Doppmann et al. 2008). This could indicate that the observed HCN, C_2H_2 and CO_2 absorption originates in a disk wind or infalling envelope rather than the disk itself. However, the high densities needed to excite these higher J-transitions as well as the constraints on the size of the high abundance region (<11 AU) imply that the absorption lines have an origin in outflowing or infalling gas that must be very closely related to the disk itself with a chemistry similar to that of the disk. This is further discussed in Lahuis et al. (2006), Gibb et al. (2007), Doppmann et al. (2008), Kruger et al. (2011) and Mandell et al. (2012). Fuente et al. (2012) recently imaged the warm HCN associated with the disk of GV Tau N at millimeter wavelengths and found an emitting radius of less than 12 AU.

Figures 10, 11 and 12 in the Appendix present C_2H_2, HCN and CO_2 absorption spectra at higher spectral resolution for $R \approx 3000$, as appropriate for the JWST-MIRI instrument, and at $R \approx 50000$, as typical for future mid-infrared spectrometers on an Extremely Large Telescope (ELT) (e.g., METIS on the E-ELT, Brandl et al. 2010). The latter spectrum is also characteristic (within a factor of 2) of the spectral resolution of $R = 100000$ of EXES on SOFIA (Richter et al. 2006) or a potential high resolution spectrometer on the SPICA mission (Goicoechea &

Nakagawa 2011). As expected, the central *Q* branch becomes deeper with higher spectral resolution and the *P*− and *R*-branches become readily detectable, allowing a more accurate model fit to the data. The inferred column density, however, should not change beyond the error bars derived from the low resolution data.

5.3.3 Other molecules

Overview

Table 5.1 summarizes the molecular data (vibrational mode, line positions, band strengths) used for all molecules for which searches have been made toward IRS 46 and GV Tau in the 10–30 μm wavelength range, together with the main references from which they have been extracted. Only the intrinsically strongest bands of each molecule have been chosen; weaker bands are ignored. Note that isotopologues and vibrationally excited states or 'hot bands' are not included in the data sets, except in the fitting of the observed spectra of HCN, CO_2 and C_2H_2. Hot bands are expected to be suppressed in full non-LTE calculations, where the excitation of the higher vibrational levels is subthermal at densities below $\approx 10^{10}$ cm^{-3}. Synthetic spectra are generated following the procedures as described in Helmich (1996), Lahuis & van Dishoeck (2000).

Our spectra use molecular data from various databases listed in Table 5.1. To assess their reliability, we have computed the integrated absorption band strengths of the simulated spectra and compared them with independent band strengths tabulated in the literature (columns 5 and 6 of Table 5.1. This table shows that the band strengths of all species agree to within factor of ~ 3 and in most cases much better. For the purpose of this paper this accuracy is sufficient and differences between databases and other literature values are not pursued here. It should be noted, however, that there are (sometimes significant) differences between line lists and not all line lists are complete.

Figure 5.3 presents an overview of the simulated LTE spectra for all molecules considered here at $T = 500$ K, $R = 50,000$ and a column density of $1 \cdot 10^{16}$ cm^{-2}. A variety of absorption patterns is seen, depending on the characteristics and symmetries of the individual bands involved. Together, they span most of the medium resolution wavelength range observed by *Spitzer*.

Upper limits from Spitzer data

To estimate the upper limits of non-detected molecules, first the rms was calculated over the region where the spectral band of the molecule of interest is expected to be. The wavelength range of this region was set to be 10 times the FWHM of the *Q*-branch of the molecule, except for SO_2 where the *P* and *R*-branches were taken as a reference point. The rms was then multiplied by 3 to assume a 3σ limit. The absorption LTE model was subsequently used to determine the maximum column

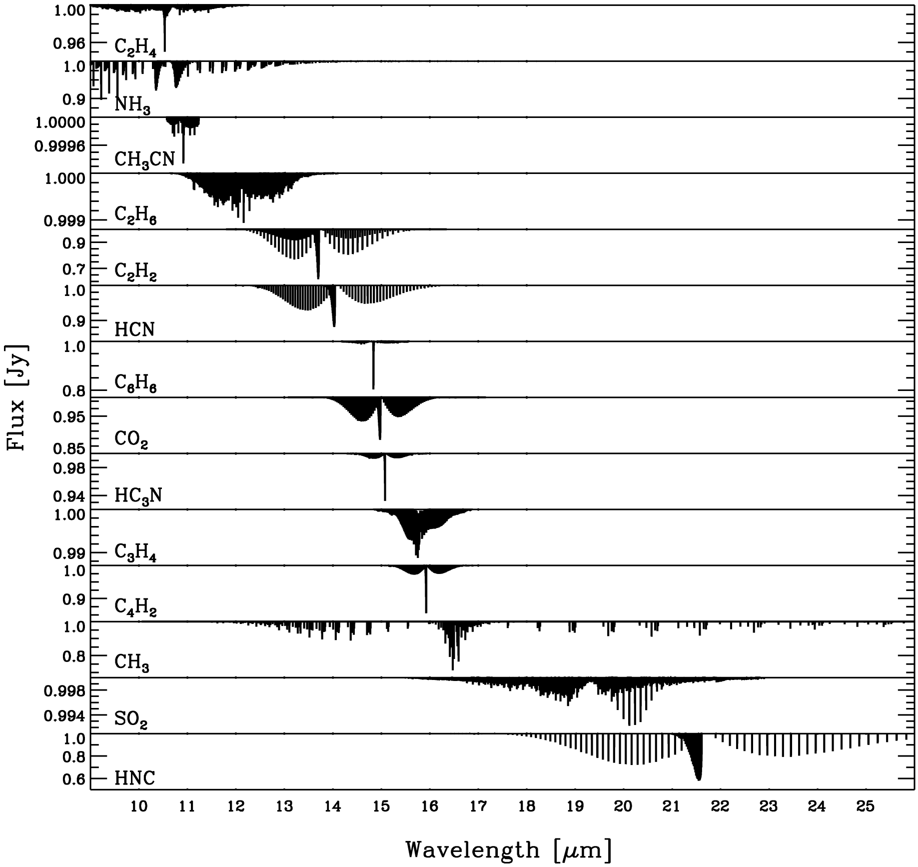

Figure 5.3 Synthetic spectra of the different molecules for T_{ex}=500 K and for a resolving power of R=50,000. The column density of each molecule is set to be $1 \cdot 10^{16}$ cm^{-2} which is the same as in Fig. 10–22

density that fits the data within the 3σ range. Three different temperatures of 200, 500 and 1000 are adopted, using $b = 5$ km s^{-1} throughout.

Plots with parts of the observed spectra for GV Tau and IRS 46 including the synthetic spectra of the different molecules set so that their Q-branch has a depth of 3σ at a temperature of 500 K are presented in Fig. 5.4 and Fig. 5.5. For reference, Figures 10 – 23 in the Appendix present an overview of the simulated LTE spectra at $R = 600$ for all the molecules considered here at additional temperatures of 200 and 1000 K.

The derived 3σ upper limits on the column densities are presented in Table 5.3 and 5.4. In addition Fig. 5.6 shows how the relative intensity in percent changes with temperature and column density for each molecule. Not all column densities follow the expected trend of a higher upper limit on the column density at a higher temperature because of a decrease in the depth of the Q-branch. This tendency can be explained when looking at the different spectra. For example, HNC follows the expected trend (Fig. 13), but not C_6H_6 (Fig. 20). The latter behavior is due to the low spectral resolving power $R = 600$ which does not resolve the intrinsically narrow Q–branch of this heavy molecule. At higher resolving power, however, the strength of Q-branch does in fact decrease with the temperature as expected.

Tables 5.5 and 5.6 present the upper limits on the column densities relative to C_2H_2 and HCN, respectively, for both IRS 46 and GV Tau. Abundance ratios relative to C_2H_2 and HCN are typically of order unity, except for CH_3CN and C_2H_6 which have particularly low band strengths (see Table 5.1). The most stringent ratios of <0.2–0.5 are obtained for C_4H_2 and C_6H_6. The ratios are also graphically displayed in Figures 5.7 and 5.8 where they are compared with model results. These results will be further discussed in §5.4.

5.3.4 High resolution spectra

Figures 13 – 21 present the higher resolution spectra of all molecules at R=3000 and 50,000 at $T_{ex} = 200, 500$ and 1000 K using $b = 5$ km s^{-1} and a column density of $1{\cdot}10^{16}$ cm^{-2}. The improved detectability of the molecules at higher spectral resolution is obvious. The resulting 3σ limits are included in Table 5.3 for IRS 46. For GV Tau, the limits at higher resolution scale similarly. The column density limits are lower by factors of 2–10. They do not decrease linearly with increasing resolving power, however, because the strong Q–branches used to set the limits are blends of many lines at low resolution which become separated at higher resolving power. In some cases (C_2H_6, CH_3CN), the gain is very small because the molecule absorbs less than 0.1% of the continuum for the adopted column density, which remains undetectable at S/N=100 even at high spectral resolution.

Tables 5.5 and 5.6 include the column density ratios with respect to C_2H_2 and HCN at higher resolving power. Since the C_2H_2 and HCN column densities remain the same, the abundance ratio limits are now up to an order of magnitude lower, thus bringing the limits in a more interesting regime where they provide more

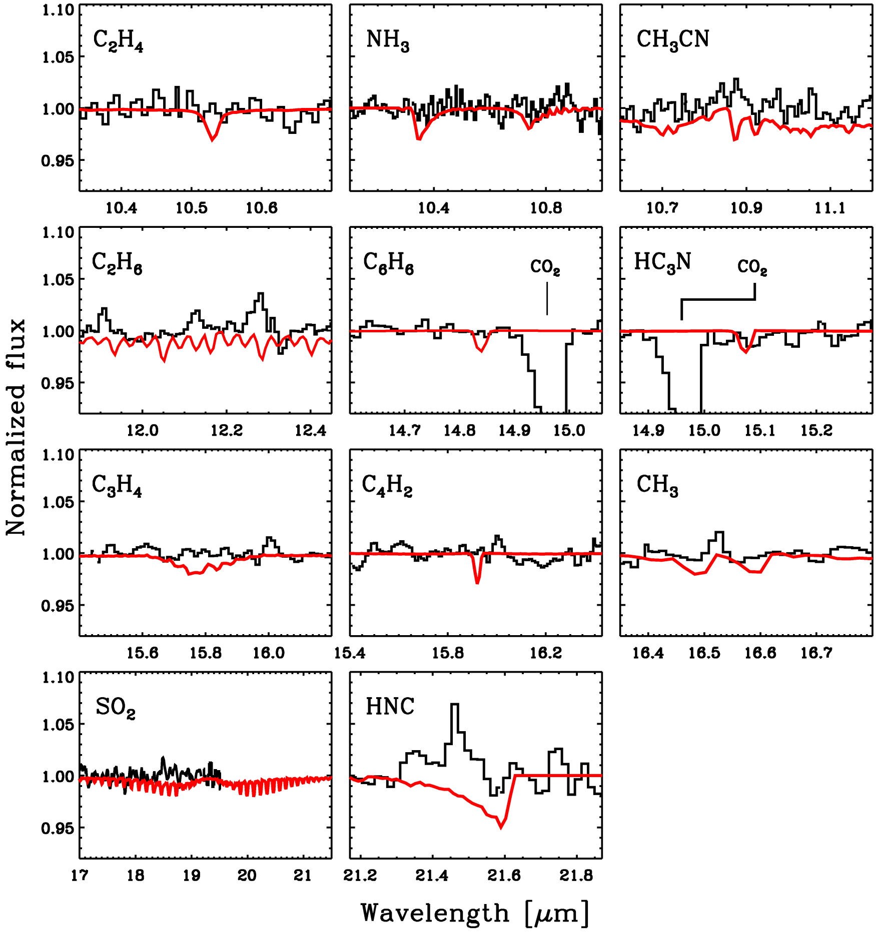

Figure 5.4 Synthetic spectra (in red) for different molecules at a 3σ maximum optical depth compared with the observed spectrum of IRS 46 (in black).

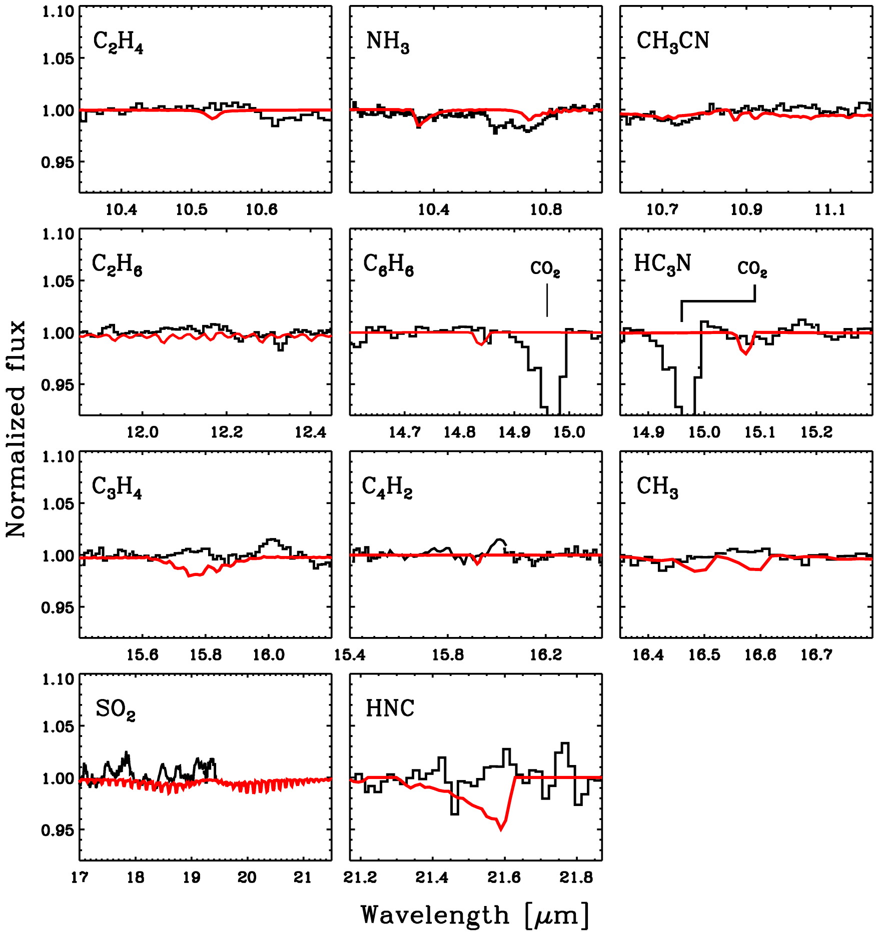

Figure 5.5 Synthetic spectra (in red) for different molecules at a 3σ maximum optical depth compared with the observed spectrum of GV Tau (in black).

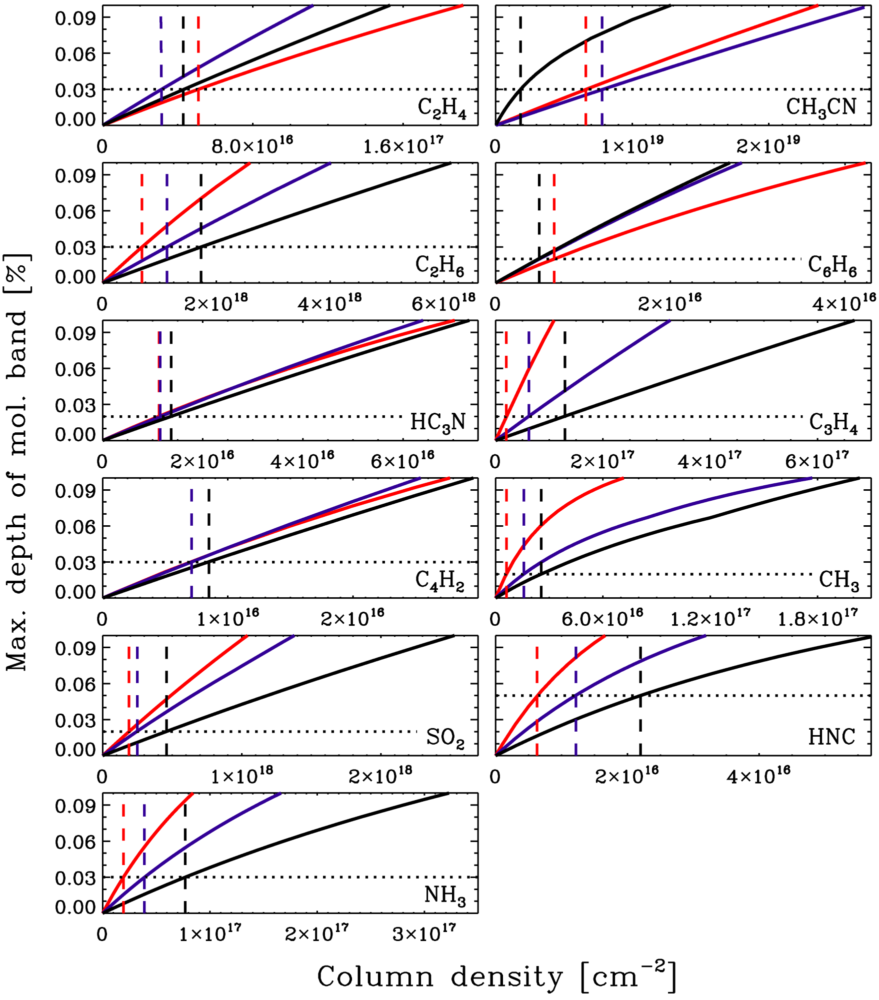

Figure 5.6 Variation of the maximum optical depth as a function of column density for different molecular bands at excitation temperatures of 200 K (red), 500 K (blue) and 1000 K (black). The 3σ observational limit for IRS 46 is marked with a black dotted line.

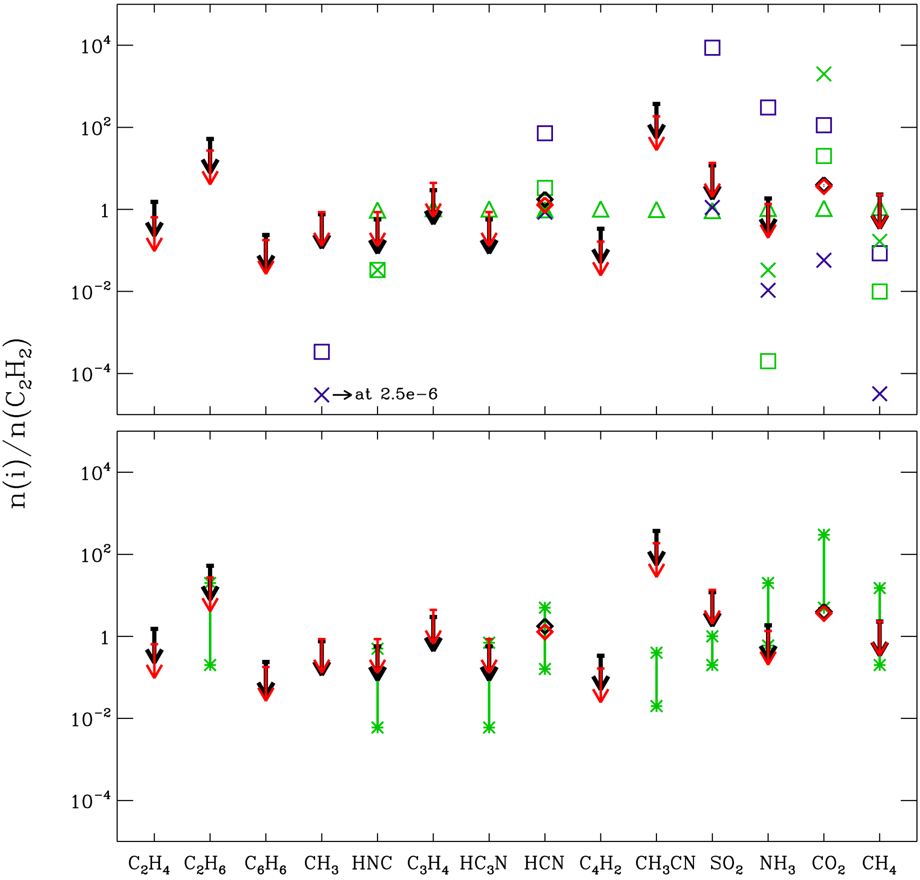

Figure 5.7 Comparison of the abundances of various species relative to C_2H_2 between inner disk observations, chemical models (upper panel) and cometary observations (lower panel). The observed upper limits for IRS 46 (black arrows) and GV Tau (red arrows) and their respective detections (black and red diamonds) are indicated. Upper panel: Abundance ratios in the disk model by Markwick et al. (2002) at 5 AU (green triangle), from the reference disk model (blue square) and for O/C = 1 (blue cross) at 1 AU by Najita et al. (2011) and from the disk model by Agúndez et al. (2008) at 1 AU (green square) and 3 AU (green cross). Lower panel: the abundance ratios detected in comets (the detection range for each molecule is indicated with 2 green stars) (Mumma & Charnley 2011).

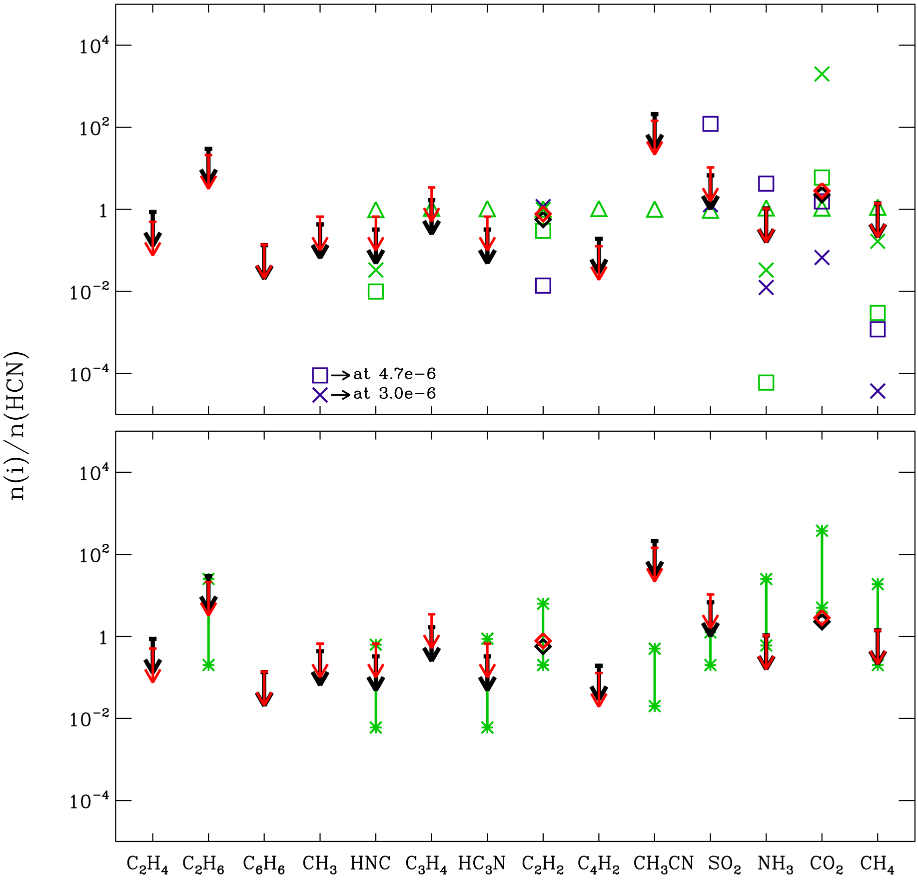

Figure 5.8 Comparison of the abundances of various species relative to HCN between inner disk observations, chemical models (upper panel) and cometary observations (lower panel). The observed upper limits for IRS 46 (black arrows) and GV Tau (red arrows) and their respective detections (black and red diamonds) are indicated. Upper panel: Abundance ratios in the disk model by Markwick et al. (2002) at 5 AU (green triangle), from the reference disk model (blue square) and for O/C = 1 (blue cross) at 1 AU by Najita et al. (2011) and from the disk model by Agúndez et al. (2008) at 1 AU (green square) and 3 AU (green cross). Lower panel: the abundance ratios detected in comets (the detection range for each molecule is indicated with 2 green stars) (Mumma & Charnley 2011).

Table 5.3 Inferred upper limits of column densities [10^{16} cm^{-2}] toward IRS 46 at different excitation temperatures and spectral resolving powers.

	C_2H_4	C_2H_6	C_6H_6	CH_3	HNC	C_3H_4
R=600, 200 K	<5.1	<69	<0.7	<0.6	<0.6	<2.0
500 K	<3.2	<110	<0.5	<1.6	<1.2	<6.2
1000 K	<4.3	<170	<0.5	<2.6	<2.2	<13
R=3000[a]	<1.8	<50	<0.2	<0.4	<0.9	<3.1
R=50,000[a]	<0.6	<29	<0.09	<0.06	<0.09	<1.8
3σ [%][b]	0.03	0.03	0.02	0.02	0.05	0.02

	HC_3N	C_4H_2	CH_3CN	SO_2	NH_3
R=600, 200 K	<1.1	<0.7	<660	<19	<2.0
500 K	<1.2	<0.7	<780	<25	<3.9
1000 K	<1.4	<0.9	<180	<46	<7.7
R = 3000	<0.4	<0.3	<310	<8.5	<1.4
R = 50,000	<0.3	<0.2	<46	<2.6	<0.3
3σ [%]	0.02	0.03	0.03	0.02	0.03

[a] The upper limits at spectral resolving powers of R = 3000 and 50,000 are for a maximum of 3σ absorption at T = 500 K.

[b] The actual 3σ limit in % absorption at the location of the molecular band.

stringent tests of chemical models.

Note that these limits do not take the transmission of the Earth's atmosphere into account but assume that the strong Q-branches can be observed unobscured. For ground-based instruments, this is often not the case and detectability depends both on the transmission and on the radial velocity shifts of the sources with respect to atmospheric lines (Lacy et al. 1989).

Table 5.4 Inferred upper limits of column densities [10^{16} cm^{-2}] toward GV Tau at different excitation temperatures at a resolving power of R=600.

	C_2H_4	C_2H_6	C_6H_6	CH_3	HNC	C_3H_4
200 K	<1.2	<23	<0.3	<0.4	<0.6	<2.0
500 K	<0.9	<38	<0.3	<1.2	<1.2	<6.2
1000 K	<0.9	<57	<0.3	<1.8	<2.2	<13
3σ [%] [a]	0.010	0.010	0.010	0.015	0.050	0.020
	HC_3N	C_4H_2	CH_3CN	SO_2	NH_3	
200 K	<1.1	<0.2	<230	<14	<0.9	
500 K	<1.2	<0.2	<260	<19	<1.9	
1000 K	<1.4	<0.3	<50	<34	<3.7	
3σ [%]	0.020	0.010	0.010	0.015	0.015	

[a] The actual 3σ limit in % absorption at the location of the molecular band.

Table 5.5 Observed molecular column density ratios relative to C_2H_2 in disks compared with different chemical models and cometary observations.

Ratio rel to C_2H_2	C_2H_4	C_2H_6	C_6H_6	CH_3	HNC	C_3H_4	HC_3N	CH_4
IRS 46	<1.5	<52	<0.2	<0.8	<0.6	<3.0	<0.6	-
GV Tau	<0.6	<27	<0.2	<0.9	<0.9	<4.4	<0.9	-
DR Tau	-	-	-	-	-	-	-	<2.3[a]
R = 3000[b]	<0.9	<24	<0.08	<0.2	<0.4	<1.5	<0.2	-
R = 50,000	<0.3	<14	<0.04	<0.03	<0.04	<0.9	<0.1	-
Markwick et al. (2002) 1 AU	-	-	-	1.0	1.0	1.0	1.0	1.1
Markwick et al. (2002) 5 AU	-	-	-	-	1.0	1.0	1.0	1.1
Najita et al. (2011) ref	-	-	-	4.0E-4	-	-	-	0.09
Najita et al. (2011) O/C = 1.0	-	-	-	2.5E-6	-	-	-	3.2E-5
Agúndez et al. (2008) 1 AU	-	-	-	-	0.03	-	-	0.01
Agúndez et al. (2008) 3 AU	-	-	-	-	0.03	-	-	0.2
Mumma & Charnley (2011)	-	0.2–20	-	-	0.01–0.5	-	0.01–0.7	0.2–15

Ratio rel to C_2H_2	HCN	C_4H_2	CH_3CN	SO_2	NH_3	CO_2
IRS 46	1.8	<0.3	<370	<11.9	<1.9	4.0
GV Tau	1.3	<0.2	<190	<13.6	<1.4	3.6
DR Tau	-	-	-	-	-	-
R = 3000	-	<0.1	<150	<4.0	<0.7	-
R = 50,000	-	<0.1	<22	<1.2	<0.1	-
Markwick et al. (2002) 1 AU	1.0	1.0	1.0	0.9	1.0	1.0
Markwick et al. (2002) 5 AU	1.0	1.0	1.0	0.9	1.1	1.1
Najita et al. (2011)	70	-	-	8700	310	110
Najita et al. (2011) O/C	0.9	-	-	1.1	0.01	0.06
Agúndez et al. (2008) 1 AU	3.0	-	-	-	2.0E-4	20
Agúndez et al. (2008) 3 AU	1.0	-	-	-	0.03	2000
Mumma & Charnley (2011)	0.2–5.0	-	0.02–0.4	0.2–1.0	0.6–20	5.0–300

[a] From 3 μm emission data (Mandell et al. 2012).

[b] The R=3000 and 50,000 values refer to the 3σ limits on the abundance ratios that can be obtained toward IRS 46 if observed at higher spectral resolution.

Table 5.6 Observed molecular column density ratios relative to HCN as well as CH_3CN/NH_3 compared with chemical models and with cometary observations.

Obs/models	HNC	HC_3N	CH_3CN	NH_3	CH_3CN/NH_3
IRS 46	<0.3	<0.3	<210	<1.1	<200
GV Tau	<0.7	<0.7	<140	<1.1	<140
AS 205	-	-	-	<2.7[a]	-
R = 3000[b]	<0.2	<0.1	<84	<0.4	220
R = 50,000	<0.03	<0.08	<12	<0.08	160
Markwick et al. (2002) at 1 AU	1.0	1.0	1.0	1.0	1.0
Markwick et al. (2002) at 5 AU	1.0	1.0	1.0	1.1	0.9
Najita et al. (2011) ref	-	-	4.0	-	-
Najita et al. (2011) O/C = 1.0	-	-	0.01	-	-
Agúndez et al. (2008) 1 AU	0.01	-	-	6.0e-5	-
Agúndez et al. (2008) 3 AU	0.03	-	-	0.03	-
Mumma & Charnley (2011)	0.01–0.6	0.01–0.9	0.02–0.5	0.6–25	0.01–0.1
Garrod et al. (2008) M	-	-	-	890	7.5E-5

[a] From 3 μm emission (Mandell et al. 2012).

[b] The R=3000 and 50,000 values refer to the 3σ limits on the abundance ratios that can be obtained toward IRS 46 if observed at higher spectral resolution.

5.4 Discussion

Tables 5.5 and 5.6 and Figures 5.7 and 5.8 compare our limits with a variety of chemical models. There are two distinct routes towards molecular complexity in regions of star- and planet formation. First, at elevated temperatures such as found in the inner disks, various reactions with activation barriers open up. If atomic carbon can be liberated from CO and atomic nitrogen from N_2, high abundances of CH_4, C_2H_2 and HCN can be produced. The second route starts in the pre-stellar cores where ices are formed through grain surface reactions. At a later stage, these ices can be transported into the disk and evaporate so that a chemistry rich in hydrogenated molecules can ensue. We review each of these classes of models and then discuss our observations in the light of these models and in comparison with cometary and other data.

5.4.1 Warm chemistry

The warm gas chemistry in the photospheres of disks follows a similar chemical scheme as that in other interstellar regions with high temperature gas such as the inner envelopes of massive protostars (e.g., Doty et al. 2002, Rodgers & Charnley 2003, Stäuber et al. 2005), high density photodissociation regions (PDRs) (e.g., Sternberg & Dalgarno 1995) and shocks (e.g., Mitchell 1984, Pineau des Forêts et al. 1987, Viti et al. 2011). In fact, high abundances of C_2H_2, HCN and CO_2 were first found in gas with temperatures of several hundred K near massive protostars (Lacy et al. 1989, Evans et al. 1991, Lahuis & van Dishoeck 2000). The chemical scheme starts with separating C or C^+ from CO and N from N_2, see Fig. 5.9 (adapted from Agúndez et al. 2008). This can be done either by UV photons, cosmic rays or X-rays. A UV-dominated region will produce comparable amounts of C^+ and C, whereas cosmic rays and X-rays produce He^+ which will react with CO to produce primarily C^+.

For carbon-bearing species, the rate limiting steps of this scheme are the reactions of C and C^+ with H_2 which have activation barriers E_a of ~12,000 and 4,000 K, respectively. At temperatures of a few hundred K, the C^+ channel leads to CH_4 and C_2H_2 while at high temperatures (>800 K), the C-channel becomes active. Reactions of C_2 with H_2 have activation barriers of ~1500 K and form another route to produce C_2H and subsequently C_2H_2. For nitrogen-bearing species, the reactions of NH with H_2 ($E_a \sim 7800$ K) to form NH_3 and of CN with H_2 ($E_a \sim 820$ K) to form HCN also require high temperatures. At low temperatures < 200 K, the above reactions are closed and C^+, C and N will be driven back to CO and N_2 through reactions involving OH. Hence, the higher the temperature the more C_2H_2, CH_4 and HCN will be produced.

Similar arguments apply to the more complex hydrocarbons studied here. In fact, high temperature, high density chemistry starting with high abundances of C_2H_2 and HCN resembles the chemistry of the atmospheres of carbon-rich evolved

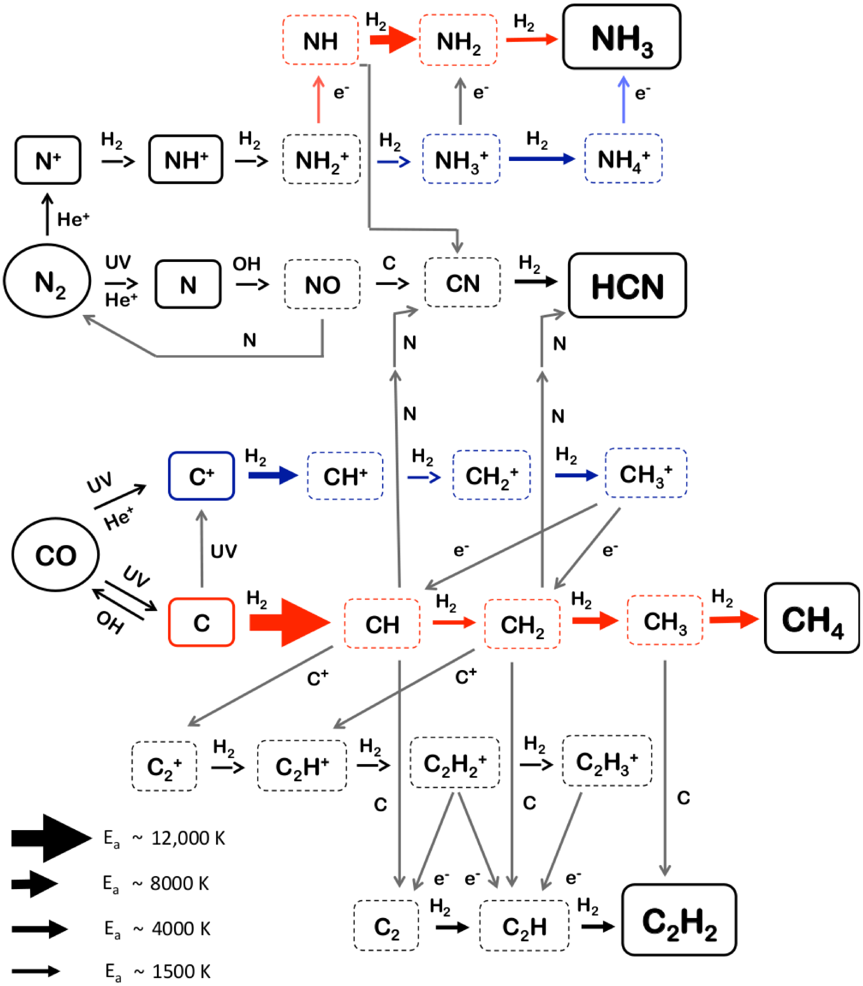

Figure 5.9 Chemical diagram describing the main reaction routes to form HCN, C_2H_2, CH_4 and NH_3 in warm gas in protoplanetary disks or hot cores depending on the radiation fields, temperature and different molecular abundances, adapted from Agúndez et al. (2008). At high temperatures of several hundred K the reaction routes (in red) starting with C reacting with H_2 to CH and NH to NH_2 dominate over lower temperature chemical routes (in blue) of C^+ going to CH^+ and NH_3^+ and NH_4^+. The different activation energy (E_a) barriers for the chemical reactions are represented by different types of arrows; the thicker the arrow, the higher the activation energy.

stars, which has been studied for decades (e.g., Cherchneff & Glassgold 1993, Millar & Herbst 1994). For example, C_2H_2 reacts with CH_3 to produce C_3H_4, with C_2H to C_4H_2, and with NH_3 to CH_3CN. If C_2H is sufficiently abundant (due to photodissociation of C_2H_2, for example), subsequent reactions may lead to large unsaturated carbon chains. More saturated molecules such as C_2H_4 and C_2H_6 need CH_4 as their starting point. Finally, nitrogen-containing species are produced by reactions of HCN or N with hydrocarbons. For example, C_2H_2 and C_2H react with HCN to form HC_3N. It is now well established that many of these neutral-neutral reactions actually have substantial rates even at low temperatures (<100 K) (Smith 2011). Thus, the bottleneck in producing the more complex organic molecules is the formation of the chemical precursors C_2H_2, HCN and CH_4.

Benzene is the most complex molecule probed here and is a precursor for building larger PAHs. One route to form benzene is through the reaction of C_3H_4 and its ion, found to be important in the inner disk chemistry in some models (Woods & Willacy 2007). Alternatively, the destruction of PAHs by high temperature gas-phase reactions inside the 'soot line' can lead to the production of small hydrocarbons, including C_2H_2 and perhaps C_6H_6 (Kress et al. 2010).

CO_2 is the product of the reaction of OH with CO. Models show that all atomic O is driven into H_2O at temperatures above ~230 K if there are no rapid H_2O destruction routes (e.g., Draine et al. 1983, Charnley 1997). The formation of OH also needs elevated temperatures, but peaks in the 100–200 K range because of the rapid reactions of OH with H_2 to form H_2O at higher temperatures. In warm gas, the CO_2 abundance follows that of OH and also peaks at 100–200 K, with a strong decrease toward higher temperatures.

In the following sections, more detailed descriptions of a few specific protoplanetary disk models are given, focussing on the simpler species.

X-ray dominated region (XDR) surface layers

Najita et al. (2011) have analyzed the chemistry of the inner (0.25–20 AU) portions of protoplanetary disks exposed to X rays. The physical structure derives from the thermochemical model developed by Glassgold et al. (2009). The thermal structure is evaluated separately for dust and gas and the surface gas temperature significantly exceeds that of the dust in the upper layers. In their model, gas and dust temperatures are decoupled for column densities less than 10^{22} cm^{-2}. If only the disk surface is considered ($N < 3 \cdot 10^{21}$ cm^{-2}), gas temperatures of 300 K are reached out to radial distances of 4 AU.

The formation of hydrocarbons in this model is triggered by X-rays which produce He^+ which liberates the C^+ from CO and N from N_2. Acetylene is subsequently produced by C and C^+ insertion reactions with small hydrocarbon radicals (Fig. 5.9). Hence, the C_2H_2 abundance is sensitive to the X-ray ionization rate. Radicals such as OH are also sensitive to X-rays. At low temperature, OH results from the recombination of H_3O^+ produced by ion-molecule reactions and its abundance scales directly with the ionization rate. The formation rate of daughter species of OH such as NO, SO, SO_2 and CO_2 is similarly increased by X-ray ionization. However, if their destruction is also dominated by He^+, their abundances are not sensitive to the X-ray ionization flux. This is the case for CO_2, for example. Note that the models of Najita et al. (2011) do not include UV photodissociation and may thus underestimate the amount of OH that could be produced from H_2O in the upper layers.

The transformation of N back to N_2 is mediated by neutral reactions and is accompanied by significant column densities of warm nitrogen-bearing molecules such as HCN and NH_3 in these models. Specifically, HCN is influenced by X-ray ionization in its formation route because it liberates N from N_2 and then N reacts with OH to form NO, with NO subsequently reacting with C to form CN. HCN is then formed through reactions of CN with H_2. Because of lack of photodissociation in the model, HCN is destroyed by He^+ and hence destruction is also sensitive to the X-ray. In the end, the HCN decreases slightly with X-ray luminosity in the models by Najita et al. (2011).

Photodissociation region (PDR) surface layers

Various recent models have analyzed the gas phase chemistry of hot inner regions of protoplanetary disks including UV radiation for the chemistry and heating of the gas (Agúndez et al. 2008, Woitke et al. 2009, Willacy & Woods 2009, Vasyunin et al. 2011, Walsh et al. 2012). The Agúndez et al. (2008) study is particularly instructive because they present models for just the photosphere of the disk, down to H_2 column densities of 5×10^{21} cm^{-2} to which the UV penetrates. In their models, FUV photons and cosmic rays produce C, C^+ and N. Atomic N is then channeled to HCN through a similar reaction routine as that described in Fig. 5.9. The C^+ leads to a rich hydrocarbon radical chemistry. However, the formation of high abundances of C_2H_2 and CH_4 requires the reaction of atomic C with H_2 to proceed which has a very high activation barrier. This reaction only proceeds in very warm gas ($T > 500$ K) forming CH. This is reflected in the radial dependence of the C_2H_2 and CH_4 columns, which reach values of $\sim 10^{16}$ cm^{-2} out to radii of ~1 AU, but then drop by orders of magnitude in the colder gas. This rapid drop with disk radius is also seen in models by other authors. In contrast, the CO_2 column increases with radius in the inner 1 AU since it favors somewhat colder gas.

Walsh et al. (2012) present a combined UV + X-ray model which shows that a correct treatment of the photodissociation is generally more important than including X-rays. For the important species considered here —C_2H_2, HCN, CO_2, CH_4 and NH_3— the column densities in the inner disk do not change measurably when X-rays are added to the UV model.

The O/C ratio and hydrocarbon abundances

There have been suggestions that the O/C ratio in the gas changes with disk radius due to migration of icy planetesimals containing a large fraction of the oxygen (Ciesla & Cuzzi 2006). Hydrocarbon abundances are very sensitive to the O/C ratio (Langer & Graedel 1989, Bettens et al. 1995, Najita et al. 2011). As expected, oxygen-bearing species such as H_2O and O_2 decrease dramatically in abundance when O/C is less than 1 because all volatile oxygen (rather than all carbon) is locked up in CO. Pure carbon species such as C_2H_2 increase in abundance by orders of magnitude while nitrogen species only change appreciably when they contain C (e.g., HCN). All of this reflects the presence of excess amounts of carbon that is available for hydrocarbon formation when $O/C< 1$. Since both IRS 46 and GV Tau show large columns of gaseous CO_2, the lines of sight through the disks probed by the mid-infrared data must pass through gas with $O/C\geq 1$.

Another parameter that may affect the abundances and the O/C ratio is the overall gas/dust ratio (e.g., Najita et al. 2011, Bruderer et al. 2012). However, comparison of the CO column density with the extinction measured from the silicate optical depth shows that this ratio is close to the interstellar value for both IRS 46 and GV Tau, indicating no significant grain growth and settling along the lines of sight through these disks (Kruger et al. 2011).

5.4.2 Surface chemistry

The more complex organic molecules such as dimethyl ether seen toward protostars are the product of an active gas-grain interaction (see Tielens & Charnley 1997, Herbst & van Dishoeck 2009,for reviews). Recent models produce these species on the grains rather than in hot gas-phase chemistry, either through direct grain surface chemistry or through mild photolysis of simple ice species resulting in radicals which then react with each other to form more complex species (Garrod et al. 2008, Öberg et al. 2009). These types of grain chemistry – either direct surface reactions or photolysis – will not result in high abundances of C_2H_2 and HCN because these species will be readily hydrogenated by H. On grain surfaces, N is quickly converted to NH_3, while in the gas phase, N flows through NO to N_2 with a slight detour to HCN. Grain surface reactions lead to very high abundances of NH_3, especially in relation to HCN. Observations and comparisons with model predictions show that also CH_4 formation is very efficient on dust grains (Öberg et al. 2008).

5.4.3 Comparison of models with observations

Table 5.5 and Figures 5.7 and 5.8 show that warm chemistry can explain the observed abundance ratios of HCN, C_2H_2 and CO_2 as well as most limits. In the Markwick et al. (2002) models, all abundance ratios are close to unity, but these ratios refer to the entire disk rather than just the surface layers. It is therefore not possible to properly test these models. The models of Agúndez et al. (2008) and Najita et al. (2011) provide column densities for just the warm surface layers, but tabulate only a limited number of species.

The inner disk models of Agúndez et al. (2008) provide the correct range of column densities and abundance ratios in the surface layers around 1 AU. At 3 AU, the C_2H_2 column has dropped dramatically due to the lower temperature and the model overproduces the CO_2/C_2H_2 ratio by a factor >100. The XDR model results given by Najita et al. (2011), for the reference case of a disk at 1 AU, agree less well with the observations than the PDR model results at 1 AU. For example the SO_2, NH_3 and CO_2 model ratios relative to C_2H_2 are several orders of magnitude higher than our observed upper limits and detections. Lowering the O/C ratio to 1 instead of 2.5 decreases the difference between the observations and the pure X-ray models but now underproduces CO_2. Further examination of chemistry in the surface layers of combined UV + X-ray models such as produced by Walsh et al. (2012) are needed to better test their effects.

The importance of grain-gas interaction for the composition of the inner regions of the disk may well be revealed by NH_3 and CH_4 searches. As mentioned in section 5.4.2, high abundances of CH_4 and NH_3 relative to HCN and C_2H_2 indicate that the chemistry in the inner part of disks could be reset due to evaporation of ices from dust grains. Table 5.6 includes the results from model M of Garrod et al. (2008). The efficiency to form NH_3 on dust grains is the main reason why NH_3/HCN and CH_3CN/NH_3 are so different in the grain surface models of Garrod et al. (2008) compared with the warm chemistry models developed by Najita et al. (2011) and Agúndez et al. (2008). Our CH_3CN/NH_3 ratio derives from two upper limits and is thus of limited value for testing models. However, our observed limit on NH_3/HCN clearly favors a low ratio for the abundances of these species, inconsistent with a significant contribution from pure grain chemistry.

The observed upper limits on the other species investigated here are often higher or comparable to what the chemical models predict. Thus, a firm conclusion from our data is that the molecular abundance ratios cannot be higher than what is predicted in the current models. However they can be lower by up to an order of magnitude, and future observations with MIRI or ELT with their higher spectral resolution can in several cases directly test the ratios given by the chemical models (see Table 5.5). Specifically, deep searches for HNC, HC_3N, C_6H_6, SO_2 and NH_3 should distinguish between models.

5.4.4 Comparison with protostars, other disks and comets

The abundance ratios of the detected molecules —HCN, C_2H_2 and CO_2— are remarkably close (within factors of two) to those observed toward high-mass protostars (Lahuis & van Dishoeck 2000), which have been interpreted with high temperature gas-phase chemistry models (Doty et al. 2002). Since our NH_3/HCN limits of <1.1 are close to the detected NH_3/HCN ratio of ~1.2 toward one high-mass protostar (Knez et al. 2009), this suggests that deeper high resolution searches for NH_3 may be fruitful.

It is also interesting to compare the two observed C_2H_2/HCN abundance ratios of 0.6 and 0.8 for IRS 46 and GV Tau respectively with the one order of magnitude lower values presented in Carr & Najita (2011) for 5 protoplanetary disks in Taurus. Those ratios have been inferred from emission lines, whereas ours come from absorption data and thus probe a different part of the disk. This would imply that the C_2H_2/HCN abundance ratios probed through our edge-on disks presented are more similar to the hot cores and comets in Fig. 12 of Carr & Najita (2011) than to their protoplanetary disks. However, Salyk et al. (2011) and Mandell et al. (2012) present C_2H_2/HCN abundance ratios of ~1 for several protoplanetary disks derived from emission data, which is about the same abundance ratio as the comet and hot core observations. Thus, different analysis methods of emission data can lead to an order of magnitude different abundance ratios.

It is interesting to further compare our inferred molecular ratios to those observed in comets, see Table 5.5 and Figures 5.7 and 5.8. The ratios tabulated for comets are presented as ranges between the highest and lowest observed ratios (Mumma & Charnley 2011), and are all within our observed upper limits and detections. This comparison suggests that some of the HCN and C_2H_2 produced by warm chemistry in the inner disk is incorporated into cold comets. However, the presence of complex organics such as dimethyl ether in high abundances in comets (see Bockelée-Morvan 2011,for a recent review) suggests that the ice chemistry route is also important for their organic inventory.

In summary, our observed ratios suggest that warm chemistry models are most relevant for explaining the observed abundance patterns. Future higher resolution observations of these molecules with JWST-MIRI and other facilities can help in answering the question to what extent warm chemistry and surface chemistry contribute to the chemical composition of the gas in the planet- and comet-forming zones of disks.

5.5 Conclusions

In this paper, mid-infrared spectra of HCN, C_2H_2 and CO_2 have been analyzed for two edge-on disks, IRS 46 and GV Tau. The high S/N data have also been used to put upper limits on the abundances of other molecules predicted to be abundant in the inner disk. The main conclusions are:

- The two disks have similar column densities and similar abundance ratios of warm HCN, C_2H_2 and CO_2. The first two molecules probe gas with excitation temperatures $T \sim 400 - 700$ K, whereas CO_2 probes somewhat cooler gas. These results are similar to those found toward massive protostars.

- No other absorption features are detected above 3σ in either source, providing upper limits on a variety of hydrocarbon molecules, NH_3 and SO_2 that are of order unity or less with respect to C_2H_2 or HCN.

- The upper limits relative to C_2H_2 and HCN are either higher or close to values given by high temperature chemistry models of protoplanetary disks. The observed NH_3/HCN limit is much lower than would be expected if the chemistry in disks would have been reset due to evaporation of icy mantles on dust grains.
- Hot chemistry disk models including both X-ray and UV radiation produce abundance ratios in better agreement with our observations than pure X-ray models.
- The observed abundance ratios in comets are within the same range as our observed ratios or upper limits. The composition of comets could therefore be partly build up from gas in the inner regions of protoplanetary disks mixed outward to the comet-forming zone.
- Future observations using higher resolution instruments on SOFIA, JWST-MIRI, SPICA or ELT will be able to detect column densities which are an order of magnitude lower than the upper limits extracted from the *Spitzer*-IRS data. Such data would provide much better constraints of the hot gas phase chemical models of the inner disk. Edge-on systems such as IRS 46 and GV Tau remain uniquely suited for this purpose.

Acknowledgements

The authors are grateful to Catherine Walsh for further information on inner disk models. JEB is supported by grant 614.000.605 from Netherlands Organization of Scientific Research (NWO). EvD and FL acknowledge support from a NWO Spinoza Grant, from the Netherlands Research School for Astronomy (NOVA) and from A-ERC grant 291141-CHEMPLAN.